ChemElectroChem

Research Article
doi.org/10.1002/celc.202201072

Chemistry Europe
European Chemical Societies Publishing

www.chemelectrochem.org

Special Collection

Understanding the Impact of Fe-Doping on the Structure and Battery Performance of a Co-Free Li-Rich Layered Cathodes

Arcangelo Celeste,*[a, b] Matteo Paolacci,[a, b] Pier Giorgio Schiavi,[a] Sergio Brutti,[a] Maria Assunta Navarra,[a, c] and Laura Silvestri*[b]

A series of Co-free Li-rich layered oxides, $Li_{1.24}Mn_{0.62-x}Ni_{0.14}Fe_xO_2$ (x = 0, 0.01, 0.02 and 0.03) has been synthetized by a self-combustion reaction. Fe doping affects either lattice structure and bonding as shown by the changes in the size of unit cell calculated from diffraction patterns and in the vibrational frequencies observed in Raman spectra. The electrochemical performance has been evaluated in a lithium cell by galvanostatic cycling: Doped samples show better capacity retention and minor decreases in the specific capacity (i.e., $Li_{1.24}Mn_{0.60}Ni_{0.14}Fe_{0.02}O_2$ can supply a specific capacity of 235 $mAhg^{-1}$ with 94% of capacity retention after 150 cycles). These positive effects originated by alterations in the point defectivity (Ni^{3+} concentration, anionic and cationic vacancies), changes in the transport properties, as showed by Cyclic Voltammetry; as well as an improved structural resilience compared to the un-doped material in postmortem analyses.

Introduction

Increasing the energy density of the current Lithium-Ion Batteries (LIBs) is still challenging. One of the biggest limitations to move forward to the next generation of LIBs is represented by the positive material.[1–4] Among the possible methods to increase the performance of cathodes, the use of anionic redox reactions has been extensively studied in the recent years.[5–9] The electrochemical mechanism of the current cathode materials is typically based on the cationic redox reaction,[1,10,11] but at high voltage it is possible to store electrons also in the anionic sublattice (i.e., oxygen in the layered oxides) to largely increase the specific capacity and, therefore, the energy of a LIB.[5,7,8]

This is the case of Lithium Rich Layered Oxides (LRLOs), that can achieve capacity values of more than 250 $mAhg^{-1}$, thanks to the involvement of oxygen redox reaction in the electrochemical process.[12–15] Generally speaking, LRLOs are a wide family of mixed metals layered oxides where lithium ions are over-stoichiometric and partially occupy atomic sites in the transition metal (TM) layers, thus replacing balanced blends of Co, Mn, Ni and other metals.

Within the LRLOs family, Co-free formulations are increasingly popular,[16–19] being cheaper and more eco-friendly materials compared to the current high-capacity cathode materials.[12–15] An example recently published from our group is $Li_{1.25}Mn_{0.625}Ni_{0.125}O_2$, an over-lithiated Ni-poor Co-free LRLO that proved excellent electrochemical performance and long cycling life stability.[20]

The reason of LRLO outstanding performance roots in its very complex and ambiguous structure.[21–23] Indeed, they show an unclear crystal identity, i.e. a monoclinic defective one-phase solid solution or two-phases (monoclinic and rhombohedral) coexisting at the nanoscale, that are indicated by two different notations in the literature, i.e. $Li_{1+x}TM_{1-x}O_2$ and $xLi_2MnO_3 \cdot (1-x)LiTMO_2$, respectively.[24] On the other hand, LRLOs suffer few drawbacks that prevent their broader application, i.e., irreversible capacity lost during the first cycle, structural changes, capacity and voltage fading upon cycling.[12,25,26]

Several strategies have been proposed to improve their electrochemical behavior, being the most popular a balanced doping of the TM blend.[27–31] In this context, also our group proved that the over-lithiation combined with Al doping could be a good strategy to mitigate the voltage decay upon cycling in battery and improve the structural stability.[32,33]

In this study, we investigate the effect of iron doping on the electrochemical and chemical-physical properties of an over-lithiated LRLO. In fact, Fe-doping helps to mitigate the draw-

[a] Dr. A. Celeste, M. Paolacci, Dr. P. G. Schiavi, Prof. S. Brutti, Prof. M. A. Navarra
Department of Chemistry
Sapienza University of Rome
p. le Aldo Moro 5, 00185 Roma (Italy)
E-mail: arcangelo.celeste@uniroma1.it
Homepage: https://www.chem.uniroma1.it/
[b] Dr. A. Celeste, M. Paolacci, Dr. L. Silvestri
Department of Energy Technologies and Renewable Sources
ENEA C.R. Casaccia
via Anguillarese 301, 00123 Roma (Italy)
E-mail: laura.silvestri@enea.it
Homepage: https://energia.enea.it/
[c] Prof. M. A. Navarra
Hydro-Eco Research Center
Sapienza University of Rome
via A. Scarpa 16, 00161 Roma (Italy)

Supporting information for this article is available on the WWW under https://doi.org/10.1002/celc.202201072

An invited contribution to a Special Collection dedicated to Giornate dell'Elettrochimica Italiana 2022 (GEI2022)

backs of LRLOs due to the stabilization of the structure through a mitigation of electronic disorder.[34–36]

Here, $Li_{1.24}Mn_{0.62}Ni_{0.14}O_2$ was used as a benchmark and the effect of Fe addition on its properties has been evaluated by replacing part of manganese with three different amounts of Fe, obtaining three new materials, namely $Li_{1.24}Mn_{0.61}Ni_{0.14}Fe_{0.01}O_2$, $Li_{1.24}Mn_{0.60}Ni_{0.14}Fe_{0.02}O_2$ and $Li_{1.24}Mn_{0.59}Ni_{0.14}Fe_{0.03}O_2$. All materials have been characterized in terms of composition, structure, morphology and, furthermore, the electrochemical behavior has been evaluated by galvanostatic cycling (GC), cyclic voltammetry (CV) and electrochemical impedance spectroscopy (EIS).

Results and Discussion

Characterization of $Li_{1.24}Mn_{0.62-x}Ni_{0.14}Fe_xO_2$ materials

The pristine and the Fe-doped samples are labeled as LRLO–F0, LRLO–F1, LRLO–F2 and LRLO–F3, according to the amount of iron in the formula, as reported in table 1. Their chemical composition has been determined by atomic absorption spectroscopy and the corresponding results are shown in table S1, confirming the excellent match between nominal and experimental stoichiometries.

Table 1. List of synthesized $Li_{1.24}Mn_{0.62-x}Ni_{0.14}Fe_xO_2$ samples and labelling adopted in the text to identify them.

Sample label	X	Formulation
LRLO–F0	0	$Li_{1.24}Mn_{0.62}Ni_{0.14}O_2$
LRLO–F1	0.01	$Li_{1.24}Mn_{0.61}Ni_{0.14}Fe_{0.01}O_2$
LRLO–F2	0.02	$Li_{1.24}Mn_{0.60}Ni_{0.14}Fe_{0.02}O_2$
LRLO–F3	0.03	$Li_{1.24}Mn_{0.59}Ni_{0.14}Fe_{0.03}O_2$

X-Ray Diffraction (XRD) patterns shown in the Figure 1a, confirm that all samples crystallize in the desired layered lattice (prototype α-$NaFeO_2$ with a rhombohedral unit cells exhibiting an R-3 m space group): also the expected few extra weak peaks are observed at 20–25°.[15,33] These latter peaks correspond to reflections of a Li_2MnO_3 phase (monoclinic C2/m space group) and their occurrence is due to the presence of lithium ions in the transition metals layers. A fully random occupancy by TM and Li^+ in the transition metals layer would result in a purely rhombohedral phase. On the other hand, the monoclinic lattice shows in the transition metals layer the formation of periodic $LiTM_6$ planar hexagonal coordination motifs (honeycomb coordination of lithium).[37–39] In LRLO the probability of the occurrence of repeated vicinal $LiTM_6$ motifs is neither null nor unitary, thus leading to an intermediate lattice where rhombohedral symmetries coexist with limited monoclinic features.[23,40] The achievement of a well-ordered layered structure is confirmed by the splitting of the (006)/(102) and (108)/(110) pair of peaks,[32,41,42] indexed by the rhombohedral structure. No phase impurity is detected by diffraction in all samples, indicating the high purity of the synthesized materials, either undoped or Fe-doped. Quantitative crystallographic information about the crystal structure has been obtained by Rietveld refinement by fitting the experimental patterns with the R-3 m unit cell. The results are shown in Figure S1 and in Tables 2 and S2. Table 2 reports lattice parameters, the c/a ratio and the volume calculated for the four materials. Overall, the iron doping leads to a lattice expansion induced by the larger ionic radium compared to Mn: these lattice expansions demonstrate the successful incorporation of iron dopants into the TM layers while preserving a well-ordered stacking along the x-axis.[41,42]

Raman Spectroscopy has been employed to investigate the surface and the local structure of the samples. Experimental results are shown in Figure 1b. All samples exhibit the same

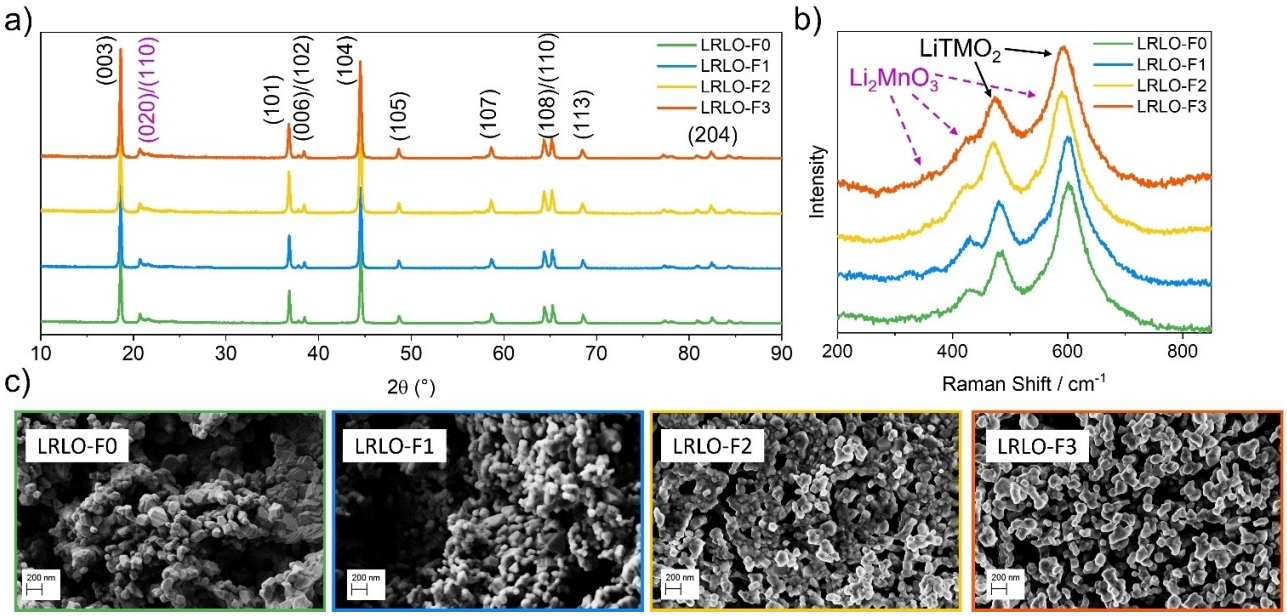

Figure 1. Comparison of a) experimental diffraction patterns, b) Raman spectra and c) Scanning Electron Microscopy (SEM) micrographs of $Li_{1.24}Mn_{0.62-x}Ni_{0.14}Fe_xO_2$ samples (x = 0–0.03).

Table 2. Lattice parameters and volumes obtained for all the samples. Rietveld refinements were performed with GSAS-II using a rhombohedral unit cell (R-3 m).

	a [Å]	c [Å]	c/a	V [Å^3]
LRLO–F0	2.857	14.269	4.995	100.86
LRLO–F1	2.858	14.272	4.993	100.97
LRLO–F2	2.860	14.279	4.993	101.16
LRLO–F3	2.861	14.278	4.991	101.21

vibrational fingerprint in line with the XRD data. Indeed, two dominant bands are observed at 600 and 480 cm^{-1}, likely assigned to the A_{1g} and E_g Raman modes of R-3 m structure ($LiTMO_2$).[43,44] Nevertheless, other modes are visible in the spectra at 560, 421, 407 and 363 cm^{-1} related to the vibrations allowed by the C2/m symmetry.[45–47]

Overall, Raman and XRD indicate that the structural features of LRLOs are maintained in the iron-doped materials.

Turning to the morphological investigation, scanning electron micrographs of the four samples are displayed in Figure 1c. All samples are constituted by polygonal particles with size between 200 and 300 nm. No significant differences among samples can be noted, thus suggesting a negligible role of iron in the crystallization process. Energy Dispersive X-ray Analysis was used to investigate the distribution of Mn, Ni and Fe within the particles, showing that all elements are evenly distributed in the selected region. The EDX maps are reported in Figure S2.

Electrochemical cycling behavior

Electrochemical performance has been investigated by galvanostatic charge/discharge measurements on lithium half coin-cells.

The first charge/discharge potential profiles were obtained under galvanostatic conditions with a current density of 20 mAg^{-1} between 2–4.95 V, and the corresponding differential capacity plots are shown in Figure 2 for all samples.

As shown from the potential profiles in Figure 2, the Li de-intercalation proceeds through two main electrochemical processes, observed as a slope up to 4.4 V and a high voltage plateau. Such electrochemical behavior is common to all LRLOs. The first process occurred below 4.4 V arises from the oxidation of transition metals as counterpart of lithium loss, while in the long plateau above 4.4 V lithium extraction is compensated by the oxidation of the oxygen in the lattice. However, the reduction mechanism follows a different path: a single process implying an incomplete reversibility due to the possibility of oxygen evolution and structural rearrangements (Figure 2).[48,49]

All samples showed the same general electrochemical mechanism, both in charge and in discharge, but the length of processes changes after the introduction of Fe. In order to evaluate the impact of iron doping, we compared the capacity associated to the two reaction steps (slope and plateau regions) in the un-doped and doped samples and the results are reported in table 3.

Table 3. Summary of specific capacities achieved by $Li_{1.24}Mn_{0.62-x}Ni_{0.14}Fe_xO_2$ series upon first charge/discharge cycle. In particular, the contribution to the capacity deriving from TM oxidation, up to 4.4 V and anion redox reaction, above 4.4 V obtained in charge have been specified.

	Charge capacity [mAhg^{-1}]			Discharge Capacity [mAhg^{-1}]
	OCV-4.4 V	4.4–4.95 V	Total	
LRLO–F0	65.88	254.74	320.62	256.5
LRLO–F1	78.89	254.5	333.40	262.9
LRLO–F2	88.47	253.93	342.4	270.66
LRLO–F3	82.70	229.01	311.71	238.9

LRLO–F0 achieves a specific capacity of ≈66 mAhg^{-1} in the sloping region and its differential capacity plot (Figure 2b) shows two oxidation peaks between 3.6 and 4.4 V, suggesting that the oxidation of Ni^{2+} to Ni^{4+} goes through the intermediate Ni^{3+}. Most of the capacity is obtained during the long plateau with a value of 255 mAhg^{-1} (Figure 2a) and a very intense anodic peak in the differential capacity plot.

As far as Fe is incorporated into the structure, the specific capacity in the slope region increases.[50,51] In fact, in the differential plot of doped materials (see Figure 2d–f–h), an increase in the intensity of the oxidation peak at about 4 V vs Li is clearly observed.

As already mentioned the redox capacities delivered in the sloping region are due only to the $Ni^{2+}/Ni^{3+}/Ni^{4+}$ couples likely increased by the Mn^{3+}/Mn^{4+} oxidation originated by possible extended oxygen defects (understoichiometry). From a purely stoichioemtric point of view, starting from the data reported in the table S1, it is possible to estimate the theoretical capacity supplied by the Ni-redox couples in the four materials: LRLO–F0 92.9 mAhg^{-1}, LRLO–F1 95.2 mAhg^{-1}, LRLO–F2 93.2 mAhg^{-1}, LRLO–F3 95.8 mAhg^{-1}. All theoretical values are above the experimental data, thus the reduced capacity in the sloping region is a clue of the presence of native Ni^{3+} centred in the pristine lattice. However the natural oxidation of nickel ions in the pristine lattice can occur in the materials preparation only under two parallel constraints: (i) the occupancy of the Li/TM and O atomic sites in the layered structure must not exceed unity, and (ii) cation and anion overall charges must be balanced to respect electroneutrality. As a consequence the presence of Ni^{3+} centres in the pristine lattice unavoidably implies the formation of native vacancies in the TM layers or in the oxygen-anionic sublattice. By assuming that the capacity delivered in the sloping region reported in table 3 is only due to the Ni^{2+}/Ni^{4+} and Ni^{3+}/Ni^{4+} oxidations, it is possible to estimate by simple stoichiometric calculations the following properties in the four samples.

- The Ni^{3+} percentage with respect to the overall nickel content in the pristine lattices (LRLO–F0 57%; LRLO–F1 33%, LRLO–F2 11%; LRLO–F3 26%)
- The percentage of vacancies in the TM layers (LRLO–F0 4.06%; LRLO–F1 2.38%; LRLO–F2 and LRLO–F3 0%)
- The percentage of vacancies in the oxygen sublattice (LRLO–F0 and LRLO–F1 0%; LRLO–F2 1.58%; LRLO–F3 0.02%)

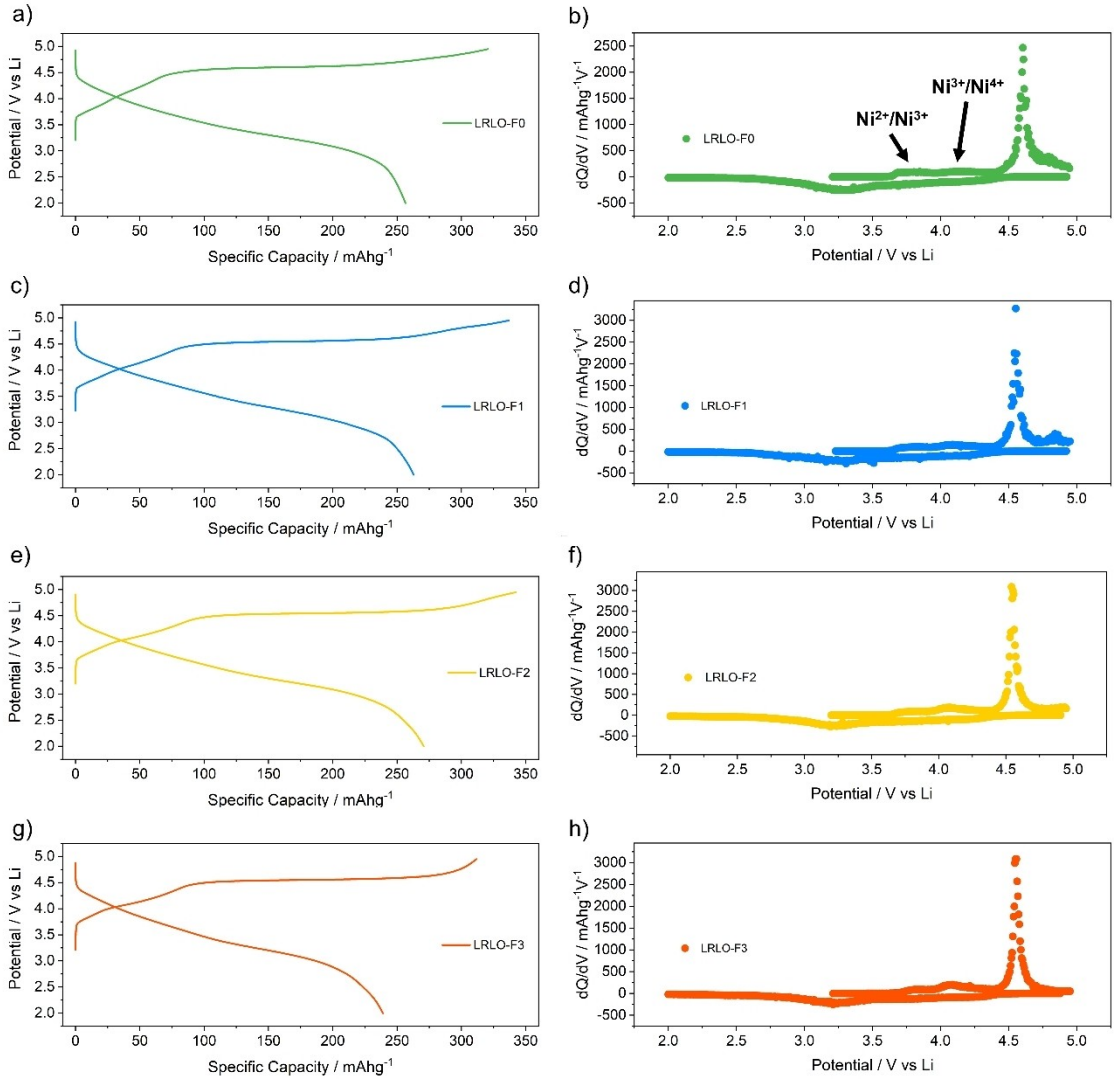

Figure 2. a,c,e,g) First charge/discharge potential profiles and the b,d,f,h) corresponding differential capacity plots of $Li_{1.24}Mn_{0.62-x}Ni_{0.14}Fe_xO_2$ series obtained in galvanostatic mode in the voltage range of 2–4.95 V, using a current density of 20 mAg^{-1} (1 C = 400 mAh/g).

The undoped materials are a p-doped LRLO compared to the ideal $Li_{1.2}Ni_{0.2}Mn_{0.6}O_2$ one, as the substitution of Ni with Li and Mn reduced the total amount of electrons in the electronic structure. This p-doping apparently results in the increase of the TM-vacancies with a parallel increase of the Ni^{3+} concentration to balance the oxygen negative charges.

Turning to the Fe-doping, from an electronic structure perspective it is an n-doping of the pristine LRLO–F0 lattice as the replacement of Mn^{4+} with Fe^{3+} ions increases the total number of electrons in the unit cell. The n-doping apparently results in a strong mitigation of the vacancies in the TM layer that nullifies in the case of LRLO–F2 and LRLO–F3. On the other hand the decrease of the vacancy concentration in the TM layer directly reflects in the Ni^{3+} content and on the oxygen occupancy that slightly decreases below unity for both LRLO–F2 and LRLO–F3. In the case of the LRLO–F2 an optimal balance is obtained among the Fe^{3+} doping, the TM vacancy reduction and the O-voids increase thus leading to a minimized percentage of Ni^{3+} that is reduced by the 80% compared to the LRLO–F0 undoped benchmark material.

Moving to the plateau region, the specific capacities slightly decrease passing from the undoped to the Fe-doped materials: this effect is larger for the LRLO–F3. The anodic peak around 4.5 V also shifts to lower potential in the doped samples compared to the pristine material. All samples showed an irreversible capacity loss during the first discharge due to the partial irreversibility of the anodic oxygen redox reaction, but still maintaining specific capacities above 230 $mAhg^{-1}$ (see Figure 2a–c–e–g). In particular, LRLO–F2 sample seems to benefit from the introduction of 0.02 equivalent of Fe, particularly in terms of discharge capacity value, reaching 271 $mAhg^{-1}$.

The cycling performance of the benchmark and Fe-doped materials have been studied by performing additional galvanostatic cycling tests at 40 mAg^{-1}. The specific capacity vs cycle number is shown for all samples in the Figure 3. The specific

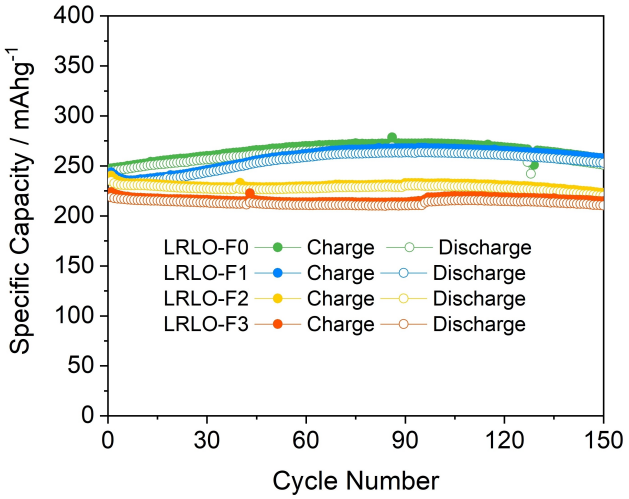

Figure 3. Specific capacity vs cycle number plots of pristine and doped samples, obtained by galvanostatic charge/discharge cycling obtained in the voltage range of 2–4.8 V, using a current of 40 mAg^{-1}. Li | LP30 | LRLO–Fx.

capacity of undoped material (LRLO–F0) is 245 $mAhg^{-1}$, during the first discharge, and it reaches a value of 251 $mAhg^{-1}$ after 150 cycles. As can be seen from the Figure, cycling performance of the pristine material shows an activated trend with an increase of the specific capacity values along cycles. Moving on the doped samples, LRLO–F1 exhibits a behavior very close to the pristine one. The capacity values are 237 and 251 $mAhg^{-1}$ at the first discharge and after 150 cycles, respectively. When the amount of Fe increases, the electrochemical performance shows relevant differences. In fact, LRLO–F2 and LRLO–F3 deliver very stable capacities upon cycling. In the first discharge, specific capacities of 235 and 219 $mAhg^{-1}$ are recorded for LRLO–F2 and LRLO–F3, respectively. Notwithstanding a slightly decrease in capacity compared to LRLO–F0 and LRLO–F1, either LRLO–F2 and LRLO–F3 demonstrated a better cyclability and capacity retention as demonstrated from the specific capacity values obtained after 150 cycles where the materials can reach 220 and 210 $mAhg^{-1}$, corresponding to the 94% and 96% of the initial capacity. As proof of the excellent behavior of $Li_{1.24}Mn_{0.62-x}Ni_{0.14}Fe_xO_2$ series, table S3 reports the comparison of the electrochemical performance of our samples with other already published Fe-doped LRLOs.

To shed additional light in the correlation between Fe-doping and electrochemical response in Li half-cells, the Li^+ ion diffusion coefficients have been measured for all samples by performing cyclic voltammetry at different scan rates. The method exploits the well-known Randles-Sevcik equation ([Eq.(1)]):

$$ip = 0.4463FAC\left(\frac{F}{RT}\right)^{1/2} n^{2/3}v^{1/2}D^{1/2} \quad (1)$$

Where *ip* represents the current peak at the specified scanning rate in Ampere, F is the Faraday constant, A is the electrode area in cm^2, *n* is the number of transferred electrons, C is molar concentration of Li^+ in the material per unit volume, v represents the scanning rate in Vs^{-1}, and D is the diffusion coefficient of Li^+.[52] The cyclic voltammetry curves are shown in Figure S3 for all samples. The voltametric peaks around 4 V vs Li, in the anodic scan, and around 3.6 V vs Li, in the cathodic scan, have been used to evaluate the diffusion coefficients, respectively in charge and in discharge. The current peaks vs the square root of the scan rate and the corresponding linear fit are shown in the Figure 4.

From the Figure, it is evident that the slope of the lines increases with the Fe addition till to LRLO–F2 sample and, then we have a drop for LRLO–F3. The detailed values are reported in table 4.

The larger values of the lithium diffusion coefficient are observed for the LRLO–F2 sample where the TM vacancies and Ni^{3+} content are minimized and, on the opposite, the oxygen vacancies and the cell volume are both maximized. Overall the motion of lithium ions during the lithiation and de-lithiation steps is facilitated by: (a) the enlargement of the lattice (volume expansion especially along the c-axis, see table 3) that widens the diffusion paths, (b) the presence of oxygen vacancies in the anion sublattice that unavoidably weaken the Li–O bonds and (c) the absence of vacancies in the TM layers that, on the opposite, strengthen the binding between TM and the oxygen-layers. Remarkably the maximization of the diffusion coefficient matches the larger delivered capacity both in the first charge and discharge processes at 20 mAg^{-1}, achieved for the LRLO–F2 sample. Furthermore, the LRLO–F2 material also shows better capacity retention at cycle 150 among all doped and undoped samples.

Stabilization of the passivation film and structural resilience induced by the Fe-doping

In order to investigate the origin of the remarkable capacity retention observed in the LRLO–F2 and LRLO–F3 samples, impedance spectra and postmortem XRD/Raman investigations have been performed.

Electrochemical impedance spectra (EIS) have been recorded in lithium half cells in the initial cycles of the galvanostatic tests at 40 mAg^{-1} at the end of discharge. The corresponding Nyquist plots recorded at cycle 5, 8, 10 and 12 are shown in the supplementary information (Figure S4). All samples exhibit the same electrochemical impedance fingerprint: the EIS response consists of a first semicircle at high-frequency, a second semicircle at medium-frequency and a straight line in the low-frequency region. The semicircle at high-

Table 4. Lithium Diffusion coefficients calculated applying the Randles-Sevcik equation to the cyclic voltammetries in Figure S4 and comparison of the values obtained in charge and discharge steps.

	D_{Li+} Charge [cm^2s^{-1}]	D_{Li+} Discharge [cm^2s^{-1}]
LRLO–F0	$7.29*10^{-12}$	$2.24*10^{-12}$
LRLO–F1	$8.48*10^{-12}$	$2.81*10^{-12}$
LRLO–F2	$1.39*10^{-11}$	$4.82*10^{-12}$
LRLO–F3	$4.9*10^{-12}$	$1.75*10^{-12}$

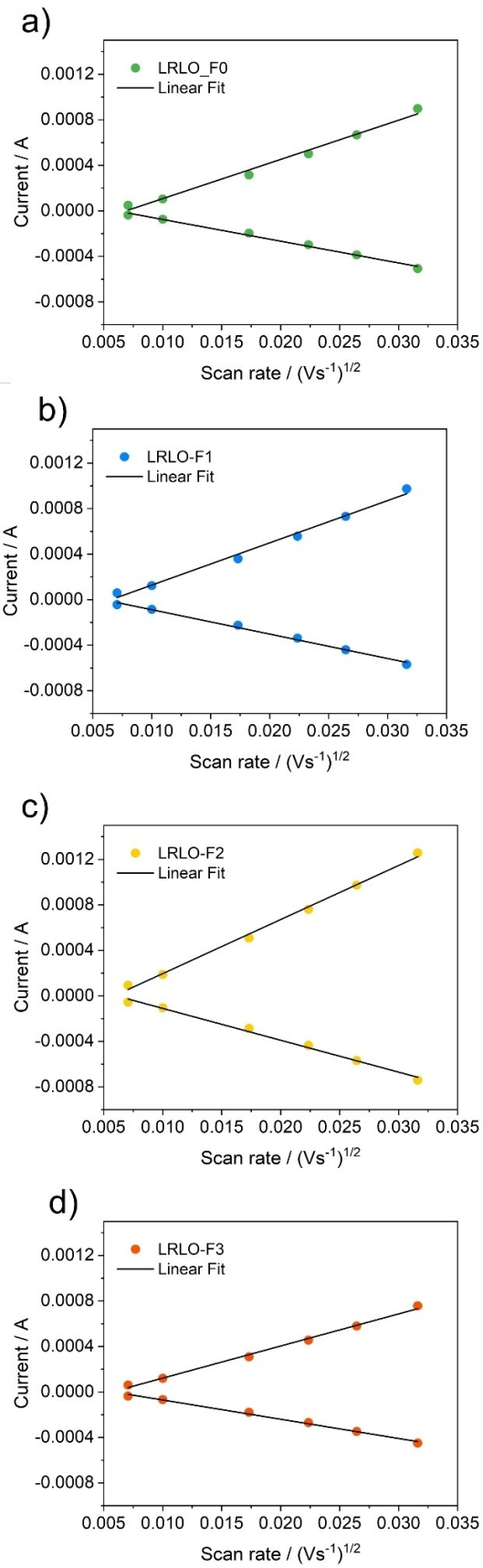

Figure 4. Peak currents vs square root of scan rates and the corresponding linear fit reported for either the charge and discharge processes. The data were obtained from cyclic voltammetries of LRLO–Fx samples carried out between 2–4.8 V with scan rates from 0.05 to 1 mV/s for the four samples.

frequency can be related to the ionic motion across the Cathode Electrolyte Interface (R_{CEI}), whereas the second semi-circle is related to the charge-transfer phenomena (R_{CT}). The low frequency line likely originated from the diffusion of lithium ions in the layered lattice. Overall, Nyquist plots showed a reduction of the semi-circle, associated to the charge transfer resistance, during the galvanostatic cycling. On the other hand, the R_{CEI} semi-circle appears almost unchanged. However, the total resistance decreases in the doped sample compared to the pristine material, suggesting the beneficial effect of the iron doping.

In order to obtain a quantitative analysis of the resistances,[53–55] the obtained EIS spectra are simulated using the equivalent circuit reported in Figure S4e and the R_{CEI} and R_{CT} values as function of cycle number have been reported for the four samples in Figure 5.

Remarkably the largest resistance values are observed at cycle 5, whereas in the following cycles both R_{CEI} and R_{CT} decrease. This trend suggests that the CEI layer over the cathodes evolves in the initial cycles of the galvanostatic test and the charge transfer process is modified during the initial de-lithiation/lithiation processes. LRLO–F2 sample shows minimal changes in both the R_{CEI} and R_{CT} thus suggesting an improved electrolyte/electrode interface with minimal degradation reactions upon cycling, stable CEI layer and, possibly, limited structural changes in the lattice.

In order to confirm the beneficial impact of a balanced iron doping on the stabilization of the layered structure during cycling, the LRLO–F2 sample has been tested in lithium half-cell by galvanostatic cycling at 1 C for 200 cycles and electrodes have been collected postmortem and analyzed by X-Ray Diffraction and Raman Spectroscopy. LRLO–F0 was used as a benchmark. *Ex-situ* XRD patterns and Raman spectra of electrodes before and after the electrochemical test are shown in Figure 6.

After 200 cycles, diffractograms of pristine and cycled materials still show sharp reflections of the layered structure with minor shifts toward smaller angles. Remarkably, peaks originated by the monoclinic distortion are almost absent in

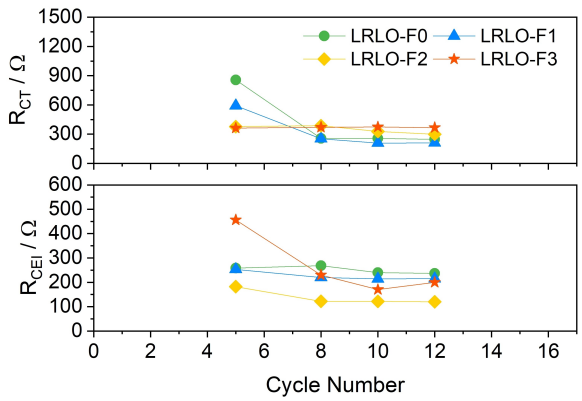

Figure 5. Evolution of the CEI and CT resistances upon cycling calculated applying the equivalent circuit in Figure S4e at Nyquist plot (Figure S4a–d) acquired with pristine and doped samples.

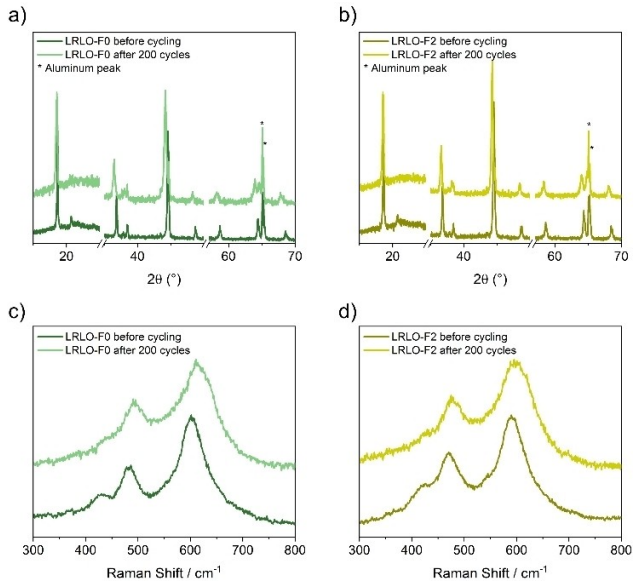

Figure 6. a–b) XRD patterns and c–d) Raman spectra acquired on LRLO–F0 and -F2 samples electrodes before cycling and after 200 cycles of galvanostatic cycling at 1 C (400 mAg^{-1}).

both samples. However, the LRLO–F2 materials shows a smaller peak shift respect to LRLO–F0, suggesting a minor expansion of the unit cell upon cycling and, therefore, a better retention of the pristine structure. On passing one may speculate that volume expansion can be directly related to the accumulation of defects in the structure, either 0D (vacancies, anti-sites, interstitials) or 2D (stacking faults) and its limitation is a clue of the preservation of the long-range LRLO ordering. Moreover, the splitting of the (006)/(102) and (108)/(110) peaks is still clearly evident in LRLO–F2, while they are more overlapped in the un-doped samples thus suggesting an improved structural resilience induced by the balanced iron doping.

Turning to the Raman spectra, only minor changes can be highlighted between the two samples. In both cases the monoclinic features are almost disappeared, in line with the observation by XRD data, but the most intense peak is still evident. Being the Raman spectroscopy a surface technique, this last evidence may suggest the possible preferential occurrence of the monoclinic distortion in proximity of the particle surface. Overall, all rhombohedral and monoclinic vibrational fingerprints are blue shifted in the spectra after 200 cycles possibly due to limited rearrangement of the local structure upon cycling. Remarkably the LRLO–F2 shows smaller blue-shift compared to LRLO–F0.

Conclusion

Four over-lithiated, Co-free LRLOs with formula $Li_{1.24}Mn_{0.62-x}Ni_{0.14}Fe_xO_2$ (x = 0, 0.01, 0.02 and 0.03) have been synthesized by the Self-Combustion method. A full chemical-physical and electrochemical characterization have been carried out with the help of several techniques (XRD, Raman Spectroscopy, SEM, CG, CV and EIS).

The layered structure and the rhombohedral/monoclinic features are maintained after the introduction of Fe, as demonstrated by XRD and Raman spectroscopy. Instead, the galvanostatic cycling revealed a slight decrease in the specific capacity values of the doped samples counterbalanced by the improvement in the capacity retention, reaching 96% in $Li_{1.24}Mn_{0.59}Ni_{0.14}Fe_{0.03}O_2$ after 150 cycles. The first charge/discharge potential profiles and the differential capacity plots clearly demonstrate the impact of the Fe-doping in the balance of 0D defects in the pristine lattice. Furthermore, the Fe-doping alters the lithium diffusion coefficient and modifies the resistance related to the CEI and the charge transfer. Overall, here we demonstrate that a balanced incorporation of Fe^{3+} doping in the LRLO lattice can improve the stability in terms of electrochemical performance, electrolyte/electrode interface and structure retention. Specifically, we reported improvements in transport properties, the charge transfer and the CEI resistances upon cycling and the structural resilience in repeated charge/discharge cycles, thus leading to enhanced electrochemical performance.

Experimental Section

Samples Preparation

Self-Combustion method was employed to synthesize pristine and doped materials. Firstly, $LiNO_3$, $Mn(NO_3)_2$*$4H_2O$, $Ni(NO_3)_2$*$6H_2O$ and $Fe(NO_3)_3$*$9H_2O$ were dissolved into an aqueous solution with the desired molar ratio. Sucrose was used as a fuel and dissolved into the metal solution. The solution was evaporated slowly by setting the temperature around 100 °C to produce a gel-like mass. Further heating at 350 °C led to the formation of precursor compound. The latter compound was grounded to get a fine and uniform powder and, then, annealed at 450 °C for 2 h (1 °C/min) and 900 °C for 12 h (10 °C/min) in air.

Material Characterization

Atomic Absorption Spectroscopy (ContrAA300 – Analytik Jena AG) was used for elemental analysis of the synthesized materials. X-Ray diffraction patterns were collected with Rigaku Smatlab diffractometer (Bragg-Brentano geometry, CuKα radiation). Crystallographic information were obtained by Rietveld refinement with GSAS-II.[56] Local structure study was performed by Raman spectroscopy by using Dilor Labram instrument, equipped with a He–Ne laser source at 632.7 nm and a CCD cooled detector. Si was used as calibrating standard for the energy scale. Morphologies were observed on Zeiss Auriga field-emission high-resolution scanning electron microscope.

Electrochemical Tests

The electrodes were fabricated by casting the samples on Al foil. The slurry for the casting was prepared by mixing positive material, SuperP and polyvinylidene difluoride (PVDF), in a weight ratio of 80:10:10, and by the addiction of N-methyl-2-pyrrolidinone (NMP). The wet film was firstly dried in a vacuum oven at 50 °C and then punched into little discs with a diameter of 10 mm. Finally, the discs

were dried in a Buchi oven overnight at 110 °C. Electrochemical tests were performed by assembling Coin Cells 2016. Lithium metal foils served as counter electrodes and glass fiber sheets (Whatman GF/A) as separator, soaked with 1 M $LiPF_6$ in ethyl carbonate (EC)/dimethyl carbonate (DMC), 1 : 1 w/w.

Galvanostatic cycling were performed on Maccor S4000 system in a voltage range of 2–4.8 V and with a current of C/10 (1 C = 400 mAg^{-1}). Before the charge/discharge test, an activation procedure was used, made of two cycles at C/10, two cycles at C/5 and other two cycles at 1 C. Cyclic voltammetries were performed using a VMP-3e Biologic workstation in a potential range of 2.0 V to 4.8 V at different scan rates and at 30 °C. Electrochemical Impedance Spectroscopy (EIS) was conducted on a VMP-3e Biologic with perturbation of 10 mV and a frequency range of 100 kHz to 10 mHz. A Dry Room with a Dew Point of −70 °C was used to prepare the electrodes and cells assembly/disassembly.

Postmortem analysis

The samples were tested by galvanostatic cycling at 1 C (400 mAg^{-1}) in lithium half-cell between 2–4.8 V. The electrodes were recovered after 200 cycles, washed in DMC several times and dried. The recovered electrodes were analyzed by XRD and Raman spectroscopy, using Rigaku Smatlab diffractometer and Dilor Labram instrument, respectively.

Acknowledgements

The authors would like to thank Dr. Francesco Mura from CNIS of Sapienza University of Rome for SEM images.

L.S. and S.B. received funds from Ministry of Ecological Transition in the framework of "Ricerca di Sistema Elettrico". S.B. and A.C. would like to thank Sapienza for the funding through the Progetto medio Bando 2021 "Idema"RM120172A46A7608.

Conflict of Interest

The authors declare no conflict of interest.

Data Availability Statement

The data that support the findings of this study are available from the corresponding author upon reasonable request.

Keywords: Co-free · Fe Doping · Li Ion Batteries · LRLO · Structure Stabilization

[1] J. Liu, J. Wang, Y. Ni, K. Zhang, F. Cheng, J. Chen, *Mater. Today* **2021**, *43*, 132–165.
[2] M. Wu, Y. Zhao, R. Zhao, J. Zhu, J. Liu, Y. Zhang, C. Li, Y. Ma, H. Zhang, Y. Chen, *Adv. Funct. Mater.* **2022**, *32*, DOI 10.1002/adfm.202107703.
[3] J. Galos, K. Pattarakunnan, A. S. Best, I. L. Kyratzis, C. H. Wang, A. P. Mouritz, *Adv. Mater. Technol.* **2021**, *6*, DOI 10.1002/admt.202001059.
[4] D. Larcher, J. M. Tarascon, *Nat. Chem.* **2015**, *7*, 19–29.
[5] R. A. House, J. J. Marie, M. A. Pérez-Osorio, G. J. Rees, E. Boivin, P. G. Bruce, *Nat. Energy* **2021**, *6*, 781–789.
[6] M. Luo, S. Zheng, J. Wu, K. Zhou, W. Zuo, M. Feng, H. He, R. Liu, J. Zhu, G. Zhao, S. Chen, W. Yang, Z. Peng, Q. Wu, Y. Yang, *J. Mater. Chem. A* **2020**, *8*, 5115–5127.
[7] P. Hou, F. Li, H. Zhang, H. Huang, *J. Mater. Chem. A* **2020**, *8*, 14214–14222.
[8] J. Xu, M. Sun, R. Qiao, S. E. Renfrew, L. Ma, T. Wu, S. Hwang, D. Nordlund, D. Su, K. Amine, J. Lu, B. D. McCloskey, W. Yang, W. Tong, *Nat. Commun.* **2018**, *9*, DOI 10.1038/s41467-018-03403-9.
[9] A. Grimaud, W. T. Hong, Y. Shao-Horn, J. M. Tarascon, *Nat. Mater.* **2016**, *15*, 121–126.
[10] A. Manthiram, J. C. Knight, S. T. Myung, S. M. Oh, Y. K. Sun, *Adv. Energy Mater.* **2016**, *6*, DOI 10.1002/aenm.201501010.
[11] F. Schipper, E. M. Erickson, C. Erk, J.-Y. Shin, F. F. Chesneau, D. Aurbach, *J. Electrochem. Soc.* **2017**, *164*, A6220–A6228.
[12] J. Wang, X. He, E. Paillard, N. Laszczynski, J. Li, S. Passerini, *Adv. Energy Mater.* **2016**, *6*, 1600906.
[13] S. Zhao, Z. Guo, K. Yan, S. Wan, F. He, B. Sun, G. Wang, *Energy Storage Mater.* **2021**, *34*, 716–734.
[14] R. J. Gummow, N. Sharma, R. Feng, G. Han, Y. He, *J. Electrochem. Soc.* **2013**, *160*, A1856–A1862.
[15] X. Ji, Q. Xia, Y. Xu, H. Feng, P. Wang, Q. Tan, *J. Power Sources* **2021**, *487*, 229362.
[16] H. H. Ryu, H. H. Sun, S. T. Myung, C. S. Yoon, Y. K. Sun, *Energy Environ. Sci.* **2021**, *14*, 844–852.
[17] N. Voronina, Y. K. Sun, S. T. Myung, *ACS Energy Lett.* **2020**, *5*, 1814–1824.
[18] Y. Yang, E. G. Okonkwo, G. Huang, S. Xu, W. Sun, Y. He, *Energy Storage Mater.* **2021**, *36*, 186–212.
[19] J. U. Choi, N. Voronina, Y. K. Sun, S. T. Myung, *Adv. Energy Mater.* **2020**, *10*, DOI 10.1002/aenm.202002027.
[20] A. Celeste, M. Tuccillo, A. Santoni, P. Reale, S. Brutti, L. Silvestri, *ACS Appl. Energ. Mater.* **2021**, acsaem.1c02133.
[21] W. E. Gent, K. Lim, Y. Liang, Q. Li, T. Barnes, S. J. Ahn, K. H. Stone, M. McIntire, J. Hong, J. H. Song, Y. Li, A. Mehta, S. Ermon, T. Tyliszczak, D. Kilcoyne, D. Vine, J. H. Park, S. K. Doo, M. F. Toney, W. Yang, D. Prendergast, W. C. Chueh, *Nat. Commun.* **2017**, *8*, 1–12.
[22] M. M. Thackeray, S. H. Kang, C. S. Johnson, J. T. Vaughey, S. A. Hackney, *Electrochem. Commun.* **2006**, *8*, 1531–1538.
[23] Y. Fan, W. Zhang, Y. Zhao, Z. Guo, Q. Cai, *Energy Storage Mater.* **2021**, *40*, 51–71.
[24] S. Muhammad, H. Kim, Y. Kim, D. Kim, J. H. Song, J. Yoon, J. H. Park, S. J. Ahn, S. H. Kang, M. M. Thackeray, W. S. Yoon, *Nano Energy* **2016**, *21*, 172–184.
[25] A. K. Shukla, Q. M. Ramasse, C. Ophus, D. M. Kepaptsoglou, F. S. Hage, C. Gammer, C. Bowling, P. A. H. Gallegos, S. Venkatachalam, *Energy Environ. Sci.* **2018**, *11*, 830–840.
[26] S. Zhao, K. Yan, J. Zhang, B. Sun, G. Wang, *Angew. Chem. Int. Ed.* **2021**, *60*, 2208–2220; *Angew. Chem.* **2021**, *133*, 2236–2248.
[27] J. Wu, H. Li, Y. Liu, Y. Ye, Y. Yang, *J. Phys. Chem. C* **2022**, *126*, 2410–2423.
[28] K. Zhang, H. Sheng, X. Wu, L. Fu, Z. Liu, C. Zhou, R. Holze, Y. Wu, *ACS Appl. Energ. Mater.* **2020**, *3*, 8953–8959.
[29] S. Dong, Y. Zhou, C. Hai, J. Zeng, Y. Sun, Y. Shen, X. Li, X. Ren, C. Sun, G. Zhang, Z. Wu, *J. Power Sources* **2020**, *462*, DOI 10.1016/j.jpowsour.2020.228185.
[30] J. An, L. Shi, G. Chen, M. Li, H. Liu, S. Yuan, S. Chen, D. Zhang, *J. Mater. Chem. A* **2017**, *5*, 19738–19744.
[31] G. Chen, J. An, Y. Meng, C. Yuan, B. Matthews, F. Dou, L. Shi, Y. Zhou, P. Song, G. Wu, D. Zhang, *Nano Energy* **2019**, *57*, 157–165.
[32] A. Celeste, F. Girardi, L. Gigli, V. Pellegrini, L. Silvestri, S. Brutti, *Electrochim. Acta* **2022**, *428*, 140737.
[33] A. Celeste, R. Brescia, G. Greco, P. Torelli, S. Mauri, L. Silvestri, V. Pellegrini, S. Brutti, *ACS Appl. Energ. Mater.* **2022**, acsaem.1c03396.
[34] Y. Xu, M. Zhang, L. Yi, K. Liang, *J. Alloys Compd.* **2021**, *865*, DOI 10.1016/j.jallcom.2021.158899.
[35] F. Wu, G. T. Kim, M. Kuenzel, H. Zhang, J. Asenbauer, D. Geiger, U. Kaiser, S. Passerini, *Adv. Energy Mater.* **2019**, *9*, DOI 10.1002/aenm.201902445.
[36] P. K. Nayak, J. Grinblat, M. Levi, O. Haik, E. Levi, D. Aurbach, *J. Solid State Electrochem.* **2015**, *19*, 2781–2792.
[37] K. Luo, M. R. Roberts, N. Guerrini, N. Tapia-Ruiz, R. Hao, F. Massel, D. M. Pickup, S. Ramos, Y. S. Liu, J. Guo, A. v. Chadwick, L. C. Duda, P. G. Bruce, *J. Am. Chem. Soc.* **2016**, *138*, 11211–11218.
[38] K. A. Jarvis, Z. Deng, L. F. Allard, A. Manthiram, P. J. Ferreira, *Chem. Mater.* **2011**, *23*, 3614–3621.
[39] C. Genevois, H. Koga, L. Croguennec, M. Ménétrier, C. Delmas, F. Weill, *J. Phys. Chem. C* **2015**, *119*, 75–83.

[40] K. Redel, A. Kulka, K. Walczak, A. Plewa, E. Hanc, M. Marzec, L. Lu, J. Molenda, *Chem. Eng. J.* **2021**, *424*, DOI 10.1016/j.cej.2021.130293.
[41] W. Zou, F. J. Xia, J. P. Song, L. Wu, L. D. Chen, H. Chen, Y. Liu, W. da Dong, S. J. Wu, Z. Y. Hu, J. Liu, H. E. Wang, L. H. Chen, Y. Li, D. L. Peng, B. L. Su, *Electrochim. Acta* **2019**, *318*, 875–882.
[42] H. Z. Zhang, Q. Q. Qiao, G. R. Li, S. H. Ye, X. P. Gao, *J. Mater. Chem.* **2012**, *22*, 13104–13109.
[43] Q. Wu, V. A. Maroni, D. J. Gosztola, D. J. Miller, D. W. Dees, W. Lu, *J. Electrochem. Soc.* **2015**, *162*, A1255–A1264.
[44] G. Sun, F. da Yu, L. F. Que, L. Deng, M. J. Wang, Y. S. Jiang, G. Shao, Z. B. Wang, *Nano Energy* **2019**, *66*, DOI 10.1016/j.nanoen.2019.104102.
[45] W. He, P. Liu, B. Qu, Z. Zheng, H. Zheng, P. Deng, P. Li, S. Li, H. Huang, L. Wang, Q. Xie, D. L. Peng, *Adv. Sci.* **2019**, *6*, DOI 10.1002/advs.201802114.
[46] D. Luo, S. Fang, L. Yang, S. I. Hirano, *ChemSusChem* **2017**, *10*, 4845–4850.
[47] Z. Yang, J. Zhong, Y. Liu, Z. Li, J. Li, K. Yang, *J. Electrochem. Soc.* **2019**, *166*, A1481–A1489.
[48] H. Chen, M. S. Islam, *Chem. Mater.* **2016**, *28*, 6656–6663.
[49] Z. Feng, H. Song, Y. Li, Y. Lyu, D. Xiao, B. Guo, *ACS Appl. Mater. Interfaces* **2022**, *14*, 5308–5317.
[50] X. Liu, T. Huang, A. Yu, *Electrochim. Acta* **2014**, *133*, 555–563.
[51] Z. Q. Deng, A. Manthiram, *J. Phys. Chem. C* **2011**, *115*, 7097–7103.
[52] T. Kim, W. Choi, H. C. Shin, J. Y. Choi, J. M. Kim, M. S. Park, W. S. Yoon, *Journal of Electrochemical Science and Technology* **2020**, *11*, 14–25.
[53] J. Pires, A. Castets, L. Timperman, J. Santos-Peña, E. Dumont, S. Levasseur, C. Tessier, R. Dedryvère, M. Anouti, *J. Power Sources* **2015**, *296*, 413–425.
[54] P. P. Dahiya, C. Ghanty, K. Sahoo, S. Basu, S. B. Majumder, *J. Electrochem. Soc.* **2018**, *165*, A3114–A3124.
[55] V. Shanmugam, S. Natarajan, L. S. Lobo, A. Mathur, M. B. Sahana, G. Sundararajan, R. Gopalan, *J. Power Sources* **2021**, *515*, DOI 10.1016/j.jpowsour.2021.230623.
[56] B. H. Toby, R. B. von Dreele, *J. Appl. Crystallogr.* **2013**, *46*, 544–549.

Manuscript received: October 27, 2022
Revised manuscript received: December 21, 2022

RESEARCH ARTICLE

Iron Doping: Small amounts of Fe in the cathode structure effectively modifiy the properties of a Co-free Lithium Rich Layered Oxides (LRLOs). Tuning of the defectivity, vacancies, and interlayer spacing with the addition of Fe leads to an improvement in the electrochemical properties: capacity retention; structural stability and resilience; lithium diffusion coefficient.

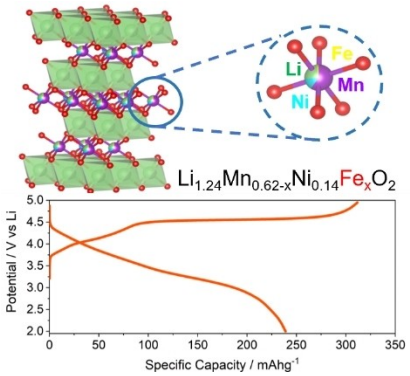

Dr. A. Celeste, M. Paolacci, Dr. P. G. Schiavi, Prof. S. Brutti, Prof. M. A. Navarra, Dr. L. Silvestri**

1 – 10

Understanding the Impact of Fe-Doping on the Structure and Battery Performance of a Co-Free Li-Rich Layered Cathodes